ELSEVIER

Journal of Nuclear Materials 249 (1997) 1–16

journal of nuclear materials

Effects of heat treatments and neutron irradiation on microstructures and physical and mechanical properties of copper alloys

B.N. Singh *, D.J. Edwards [1], M. Eldrup, P. Toft

Materials Research Department, Risø National Laboratory, DK-4000 Roskilde, Denmark

Received 14 March 1997; accepted 4 June 1997

Abstract

Tensile specimens of Cu–Al_2O_3, CuCrZr and CuNiBe alloys were given different heat treatments and then irradiated with fission neutrons at 250°C to a dose level of ≃ 0.3 dpa. Both unirradiated and irradiated specimens were tensile tested at 250°C. The microstructure and electrical resistivity were determined in the unirradiated as well as irradiated conditions. The post-deformation microstructure and fracture surfaces were also investigated. The main effect of the bonding thermal cycle heat treatment was a slight decrease in the strength of CuCrZr and CuNiBe alloys. The strength of CuAl-25, on the other hand, remained almost unaltered. The post-irradiation tests at 250°C showed a severe loss of ductility in the case of CuNiBe alloy. The irradiated CuAl-25 and CuCrZr specimens, on the other hand, exhibited a reasonable amount of uniform elongation. The results are briefly discussed in terms of thermal and irradiation stability of precipitates and particles and irradiation-induced segregation, precipitation and recovery of dislocation microstructure. © 1997 Elsevier Science B.V.

1. Introduction

Because of their good thermal conductivity, copper alloys are being considered as heat sink materials for both first wall and divertor components of ITER (International thermonuclear experimental reactor) [1,2]. The heat sink materials will have to be joined to the first wall and divertor materials at relatively high temperatures (900–1000°C). During the joining process at these high temperatures, the microstructure of precipitation hardened (PH) alloys may change substantially. Consequently, these alloys may loose swelling resistance and become softer. The oxide dispersion strengthened (ODS) copper alloys (e.g., GlidCop CuAl-25), on the other hand, are not expected to suffer from these problems since the alumina particles which are the source of strengthening, as well as swelling resistance, are thermally stable. In addition, it has been demonstrated experimentally that the alumina particles are stable against irradiation-induced dissolution [3–5].

For the reasons mentioned above, the ODS copper alloys were chosen at the ITER Technical Meeting (Garching, December 1994) to be the primary candidate materials for their use in the first wall as well as divertor components of ITER. At the same meeting it was also agreed that a backup alloy should be selected from the two well known PH copper alloys, namely CuCrZr and CuNiBe. It was therefore decided to carry out screening experiments to simulate the effect of bonding and bakeout thermal treatments on pre- and post-irradiation microstructures, mechanical properties and electrical resistivity of CuCrZr and CuNiBe alloys. On the basis of the results of these experiments, one of the two alloys should be then selected as a backup material. It was further decided that these screening experiments should be carried out at 100, 250 and 350°C so that the operational temperature range for the first wall and divertor components of ITER is properly covered. A displacement dose level of 0.3 dpa (NRT) was chosen so that the appropriate irradiation experiments, post-irradiation tests and their analysis could be completed

* Corresponding author. Tel.: +45-46 775 709; fax: +45-46 775 758.

[1] Permanent address: Structural Materials Research Section, Pacific Northwest National Laboratory, Richland, WA 99352, USA.

PII S0022-3115(97)00184-0

within a relatively short time available. Furthermore, the dose level of 0.3 dpa is considered to be reasonably representative of the dose level expected to be reached during the first phase of the ITER operation. The present paper describes the main results of these investigations at 250°C; the results of screening experiments carried out at 100 and 350°C will be reported later. The effects of bonding thermal cycles on different properties of ODS copper alloy, GlidCop CuAl-25, were investigated in the unirradiated as well as irradiated conditions. The results of these investigations are also described in the present report.

2. Materials and experimental procedure

The materials used in the present investigations were oxygen-free high conductivity (OFHC) copper, CuCrZr, CuNiBe and Cu–Al_2O_3 alloys. The OFHC–copper, CuCrZr and CuNiBe alloys were supplied by Tréfimétaux (France) in the form of 20 mm thick plates. The oxide dispersion strengthened copper (Cu–Al_2O_3) was supplied by SCM Metals (USA) with trade mark GlidCop CuAl-25 in the form of rods in the as-extruded (i.e., wrought) condition. Henceforth, the ODS copper (Cu–Al_2O_3) will be referred to as CuAl-25. The chemical composition of these alloys is listed in Table 1.

Sheet tensile specimens were cut from cold-rolled ($\simeq$ 80%) sheets ($\simeq$ 0.3 mm thick) of OFHC–copper, CuCrZr and CuNiBe alloys. Prior to irradiation, sheet tensile specimens of OFHC–copper were annealed at 550°C for 2 h in vacuum ($<$ 1.33 mPa or 10^{-5} Torr). Round tensile specimens of CuAl-25 (of gauge diameter 3 mm) were machined from the as-supplied rod, which was is in the as-wrought condition (i.e., without cold-work). The dimensions and geometry of the tensile specimens are described in [6].

For the screening experiments, the tensile specimens of CuCrZr and CuNiBe were given the following four different heat treatments (prior to irradiation): (i) solution annealing, (ii) prime aging, (iii) bonding thermal treatment and (iv) bakeout thermal treatment. The bonding thermal heat treatment for CuAl-25 specimens consisted of annealing at 950°C for 30 min (referred to as heat treatment D). The bakeout treatment was not given to the CuAl-25 since it is well known that this temperature has little effect on microstructure and properties of the alloy. All heat treatments were carried out in vacuum ($<$ 1.33 mPa). Details of the various heat treatments are summarized in Table 2.

Table 1
Chemical composition

OFHC–Cu:	Cu–10, 3, $<$1 and $<$1 ppm of Ag, Si, Fe and Mg, respectively
CuCrZr:	Cu–0.8% Cr, 0.07% Zr, 0.01% Si
CuNiBe:	Cu–1.75% Ni, 0.45% Be
CuAl25	Cu–0.25% Al as oxide particles (0.46% Al_2O_3)

The average grain size ranges from 16–22 μm in the CuNiBe, whereas for the CuCrZr the average grain size is approximately 27 μm for the HTE and HTB (see Table 2) conditions, and 45 μm for the HTC condition. The grain structure in the CuCrZr is fairly equiaxed with a narrow range of grain sizes. The CuNiBe, on the other hand, is characterized by a much broader size distribution of equiaxed grain, and many of the grains in all three conditions examined possess annealing twins. The CuAl-25, not shown here, has a grain size too small ($<$ 1 μm) to reliably measure using optical metallography.

Tensile specimens of pure copper, CuCrZr, CuNiBe and CuAl-25 alloys with the different heat treatments were irradiated at 250°C in the DR-3 reactor at Risø in the High Temperature Rig. During irradiation, temperature was measured, controlled (within $\pm$2°C) and recorded continuously. All specimens were irradiated at the same time to a fluence level of 1.5×10^{24} n/m^2 ($E > 1$ MeV), which corresponds to a displacement dose level of $\simeq$ 0.3 dpa (NRT). The neutron flux during irradiation was approximately 2.5×10^{17} n/m^{2}s ($E > 1$ MeV) which corresponds to a displacement damage rate of $\simeq 5 \times 10^{-8}$ dpa (NRT)/s.

Both unirradiated and irradiated tensile specimens were tested in an Instron machine at a strain rate of 1.2×10^{-3} s^{-1}. Tensile tests were carried out at 250°C in vacuum. The test temperature of 250°C was reached within 30 min. The cross-head displacement was measured and used to determine the stress–strain behavior of the specimens.

For transmission electron microscopy (TEM) investigations, 3 mm discs were punched from the unirradiated and irradiated sheet tensile specimens and thinned mechanically to $\simeq$ 0.1 mm thickness. The TEM specimens from the as-wrought CuAl-25 round tensile specimens were cut from the gage sections perpendicular to the tensile axis, and thinned mechanically to $\simeq$ 0.1 mm. These discs were then twin-jet electropolished in a solution of 25% perchloric acid, 25% ethanol and 50% water at 11 V for about 15 s at $\simeq$ 20°C. Specimens were examined in a JEOL 2000 FX transmission electron microscope. The fracture surfaces of the irradiated as well as unirradiated specimens were examined in JEOL 840 scanning electron microscope.

All analyses of stacking fault tetrahedra (STF) density and size distribution were performed on micrographs taken in a $(g, +4g)$ or $(g, +5g)$ weak beam dark field (WBDF) condition approximately 8° off the $\langle 011 \rangle$ zone axis, with $g = [200]_{Cu}$ the operating diffraction condition. This applied to CuAl-25, CuNiBe and CuCrZr. The micrographs were taken in regions near the edge of the foil $\simeq$ 15–25 nm in thickness. Thickness was determined by counting WBDF fringes. All measurements were taken from micrographs with a total magnification of at least 600 000.

Table 2
Summary of bonding and bakeout heat treatments for CuCrZr, CuNiBe and CuAl-25 alloys

Type	Heat treatment
A	solution annealing at 950°C for 1 h followed by water quench
E	prime aging: heat treatment A + aging at 475°C for 30 min followed by water quench
B	bonding thermal cycle: heat treatments A + E + annealing at 950°C for 30 min followed by furnace cooling + re-aging at 475°C for 30 min followed by furnace cooling
C	bakeout thermal cycle: heat treatment B + annealing at 350°C for 100 h followed by furnace cooling
C′	bakeout thermal cycle: heat treatment E + annealing at 350°C for 100 h followed by furnace cooling
D	annealing at 950° C for 30 min. (only for CuAl-25)
D′	CuAl-25 in the as-wrought condition, i.e. without any heat treatment

The analysis of the oxide particles in CuAl-25 was performed concurrently with the stacking fault tetrahedra analysis from the same images. All particles are visible in a $g = [200]$ condition (WBDF) because of the cube-on-cube orientation relationship between the alumina particles and the copper matrix.

The analysis of precipitates in CuNiBe was also obtained using a $g = [200]$ DF diffracting condition. All measurements for the precipitate density were multiplied by a factor of 3 to account for the three distinct [100] habit planes that the precipitates lie on. Measurements were made at magnifications of 600 000 or higher because of the small size of the G–P zone type precipitates. These precipitates were imaged in the two-beam dark field condition because of the strong strain field contrast, which made weak beam dark field imaging impractical.

The precipitate analysis in the CuCrZr was done by imaging the [200] or [220] reflection near the ⟨011⟩ zone axis in WBDF (g, $+4$ or $+5g$). Measurement of the precipitate density were taken from images using the [200] reflection only. The precipitate and SFT analyses were done on the same images.

All resistivity measurements were made at room temperature (23°C), using one of the modules in the A1931a Temperature Controller developed by the Electronics Department at Risø. The average resistivity of OFHC–copper (annealed at 550°C for 2 h) was found to be 1.682 $\mu\Omega$ cm, which is in good agreement with the nominal resistivity of copper at room temperature of 1.698 $\mu\Omega$ cm. The relative resistivity (RR) of the alloys was calculated from the following relationship: $RR = R \times t \times w/(R_{Cu} \times t_{Cu} \times w_{Cu})$, where R is the electrical resistance measured for the specimen of thickness t and width w. The index Cu refers to the values for the reference OFHC–Cu sample.

3. Experimental results

3.1. Pre-irradiation microstructure

In order to establish the influence of various heat treatments on different components of pre-irradiation microstructures, specimens of CuCrZr, CuNiBe, and CuAl-25 were investigated using transmission electron microscopy (TEM). In the following, the main features of the microstructure for each alloy are described.

3.1.1. CuNiBe

The solution annealed specimen (HTA) of CuNiBe showed a rather clean microstructure containing relatively

Table 3
Precipitate and particle densities in copper alloys with pre-irradiation heat treatments A, E, B, C, C′ and D. Alloys were irradiated at 250°C to a dose level of ~ 0.3 dpa. The defect cluster density was not affected by pre-irradiation heat treatments

Materials	Pre-irradiation precipitate density ($10^{23}/m^3$)						Post-irradiation precipitate density ($10^{23}/m^3$)				Defect cluster density ($10^{23}/m^3$)
	A	E	B	C	C′	D	A	E	B	D	
CuCrZr	–	0.59 (2.9 nm) [a]	0.36 (2.3 nm) [a]	–	0.51	–	0.62	0.4 (5.5 nm) [b]	0.55 (4.0 nm) [b]	–	1.0–1.6 [c]
CuNiBe	–	18 (3.8 nm) [d]	14 (6.6 nm) [d]	13	13	–	4.5	13 (4.0 nm) [d]	6.9 (5.0 nm) [d]	–	–
CuAl-25	–	–	–	–	–	0.88 [e]	–	–	–	0.18 [f]	0.43

[a] Average size as given is from the measurement of the line of no contrast present for the small spherical precipitates possessing the lobe–lobe contrast. See Section 3.1.2 for details.
[b] Average size is measured from incoherent precipitates. See Section 3.2.2 for details.
[c] In specimens with heat treatment A.
[d] Average precipitate length.
[e] Refers to density of Al_2O_3 particles.
[f] Low density is due to heterogeneity in the material, not to irradiation.243

few grown-in dislocations and only large particles that formed during solidification and/or solution annealing. The particles contained primarily nickel and some copper (Be was not detected using EDS) with a morphology ranging from cuboidal to polygonal in appearance. Guha [7] observed cuboidal particles in an earlier study on CuNiBe, and identified them as an ordered cubic B2 phase, similar to the equilibrium γ-phase observed in binary Cu–Be alloys. According to Guha, this phase formed during the high temperature solution anneal, and was highly resistant to thermal dissolution or coarsening during subsequent anneals near the melting point of copper. In addition to this phase, Guha also reported that a separate phase formed during solidification, a primary beryllide with an ordered B2 structure with a slightly larger lattice parameter (0.279 nm vs. 0.265 nm) than the cuboidal phase. The main difference between these two types of particles is that the cuboidal phase contained 50–75% more nickel than the primary beryllide. Electron diffraction identified only the cuboidal phase in this study, however, only a limited number of particles were examined. EDS did not reveal any difference in compositions between particles, but again only a few particles were examined.

Prime aged specimens (HTE) of CuNiBe contained a high density of small precipitates (Fig. 1a), with the density of precipitates approximately 30 times higher than that measured in the CuCrZr (see Table 3). Size distributions are shown in Fig. 2 for the γ″/G–P zones in both the unirradiated and the irradiated specimens. Further details on the precipitates will be presented below. The large inclusions remain in the prime aged specimens, with no discernible change in appearance after aging. Denuded zones were present along the grain boundaries in the prime aged CuNiBe (Fig. 1b), with an average zone width of ≃ 20–30 nm. Denuded zones (without any visible precipitates) were also present around the primary nickel-rich

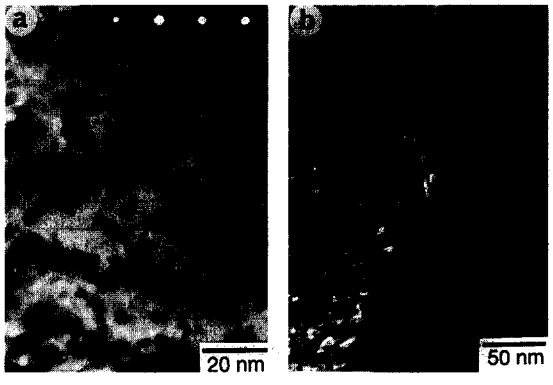

Fig. 1. Microstructure of the prime aged CuNiBe (HTE) in the unirradiated condition showing (a) the fine precipitates formed during aging and (b) the narrow denuded zone at the grain boundary. Note the presence of streaking in the diffraction pattern, a result from the thinness of the G–P zones.

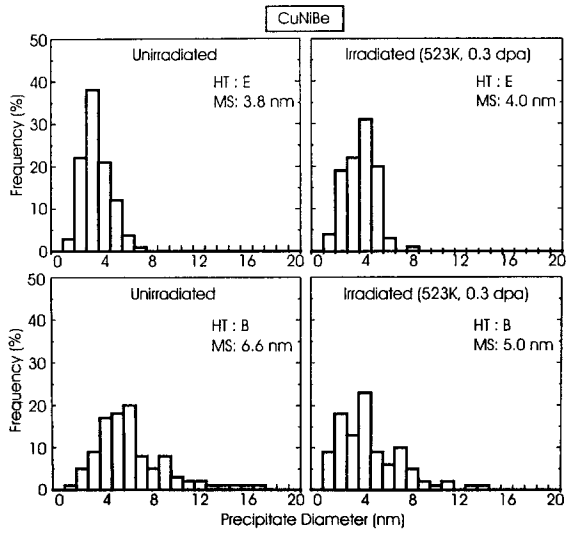

Fig. 2. Size distributions of the G–P zones and γ″ precipitates in the unirradiated and irradiated CuNiBe alloy in the HTE and HTB conditions. Note that the bonding thermal cycle (i.e., HTB) causes a noticeable amount of precipitate coarsening. The irradiation, on the other hand, does not seem to cause any significant amount of coarsening.

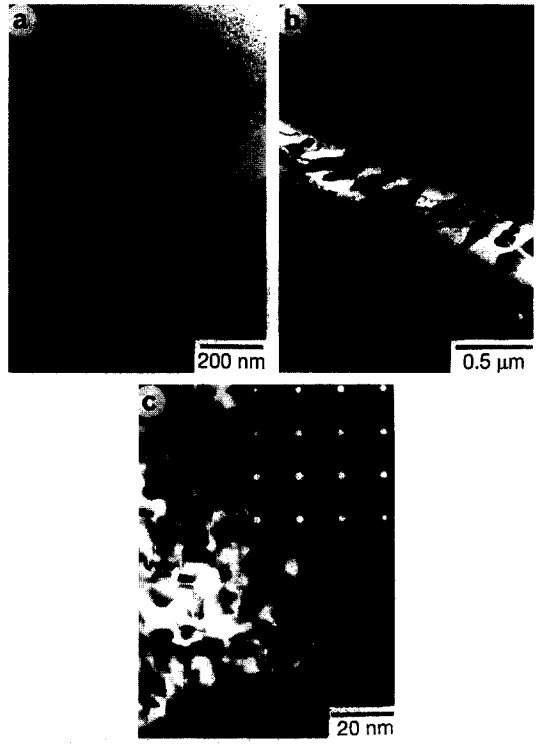

Fig. 3. Microstructure of the unirradiated CuNiBe (HTB) showing (a) wide denuded zones along a grain boundary, and (b) an extensive precipitation at a grain boundary. The G–P zones in the grain interior can be clearly seen in (c).

particles. The denuded zones in this heat treatment and the HTB treatment were characterized by a sharp transition in the precipitate density that delineates the edge of the denuded zone.

The additional bonding thermal treatment (HTB) given to CuNiBe produced significant changes in the microstructure of CuNiBe. The large primary particles were not noticeably affected by the additional heat treatment, however, denuded zones were easily visible around the particles. The denuded zones along the grain boundaries in CuNiBe (e.g., Fig. 3a) were typically 100–250 nm in width. Extensive precipitation occurred at the grain boundaries as well as in the interiors of the grains (Fig. 3b, c). Denuded zones were also present around the newly formed precipitates in the grain interiors, which were found to be Ni-rich using EDS. The precipitates at the boundaries (Fig. 3b) tended to be long, thin irregular platelets (50–500 nm long) that were closely spaced together. These long precipitates at the grain boundaries and in the grain interiors are thought to be γ-phase, an equilibrium precipitate phase in both binary CuBe and ternary CuNiBe alloys.

The bonding thermal cycle (HTB) also yielded a larger precipitate size in the CuNiBe, giving an average precipitate length of 6.6 nm as opposed to 3.8 nm in the HTE condition. The density of these precipitates (Table 3) was slightly less than that measured in the HTE specimens, but still dominated the microstructure. The HTC bakeout treatment (350°C for 100 h) did not lead to any noticeable changes in the microstructure of the HTB specimens, but the data provided in Table 3 show that the long term bakeout (HTC′) lowered the precipitate density in the HTE specimens. In addition, the denuded zones along the grain boundaries increased in width from $\simeq 20$ nm to $\simeq 100$ nm, with more particles visible on the boundaries (Fig. 4).

Guha [7] discussed the precipitation reactions that occur in CuNiBe alloys. Essentially, the addition of nickel raises

Fig. 4. Example of grain boundary denudation in the CuNiBe with the heat treatment HTC′.

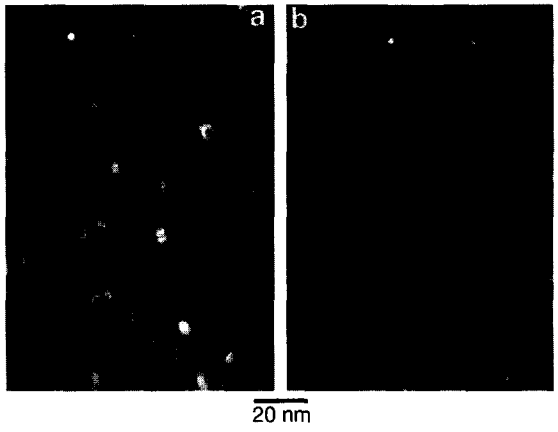

Fig. 5. Small precipitates are formed in the unirradiated CuCrZr given the HTE and HTB treatments. The micrographs in (a) and (b) are for the HTE specimens imaged on the $[220]_{Cu}$ and $[200]_{Cu}$ reflections, respectively.

the metastable solvus temperatures, allowing the formation and retention of metastable phases at higher temperatures. In this investigation the primary strengthening precipitates in CuNiBe is a mixture of Guinier Preston (G–P) zones and γ″-phase precipitates. Both phases possess a (100) habit plane relationship, and appear as thin disks when imaged near a ⟨001⟩ or ⟨011⟩ type zone axis in copper. The diffraction pattern from the HTE (e.g., Fig. 2a) and HTB specimens demonstrates that the strong streaking that occurs in the ⟨001⟩ directions is due to the thinness of the G–P zones [6]. The strong streaking in the diffraction patterns obscures the reflections at $g = \frac{2}{3}(200)$ caused by the γ″-phase. The distinction between these two phases in the images is difficult, and can only be found in the diffraction patterns if enough coarsening has occurred to reduce the streaking and produce the intensity maxima at the $g = \frac{2}{3}(200)$ position. Guha indicated that the G–P zones are much smaller than the γ″-phase ($\simeq 5$ nm vs. 10–15 nm), but this is not a clear indicator of when γ″-phase is present. The aging experienced by the CuNiBe during the bonding thermal cycle exposure did not eliminate the G–P zones based on the presence of streaking in the diffraction patterns, so the fraction of γ″-phase cannot be determined. The average size of the γ″-phase/G–P zones in CuNiBe was larger than each of the precipitate types in CuCrZr, and the strain field considerably stronger around the precipitates in CuNiBe.

3.1.2. CuCrZr

The solution annealed CuCrZr exhibited large grains with stringers of chromium-rich (bcc-Cr) particles that presumably formed during the initial processing of the alloy [6]. The particles may have formed during the solidification of the alloy. The large particles were not noticeably affected by the additional bonding thermal treatment

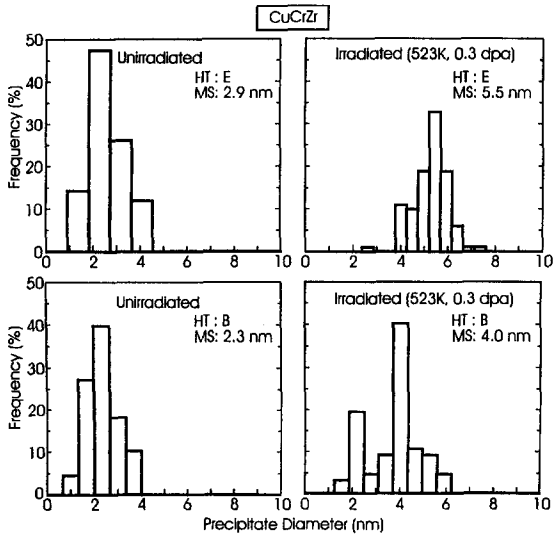

Fig. 6. Size distributions of the precipitates in CuCrZr with HTE and HTB conditions. Clarification on the types of precipitates measured is given in the text (Section 3.1.2). Note that the bonding thermal cycle (i.e., HTB) does not cause any noticeable precipitate coarsening. The irradiation, on the other hand, causes a significant amount of coarsening.

(HTB) or the prime aging (HTE). No denuded zones at the grain boundaries were observed in the prime aged CuCrZr, and their presence around the Cr-rich particles could not be determined since the copper matrix surrounding the inclusions tended to polish away during specimen preparation.

Both the prime aging and the bonding thermal treatment yielded a fine scale precipitate structure (Fig. 5), the details of which will be presented below. The size distributions of the precipitates in CuCrZr with HTE and HTB are shown in Fig. 6. No precipitate denuded zones were present along the grain boundaries. Unlike in the case of CuNiBe (HTB), no additional large scale precipitation was observed at the grain boundaries or in the grain interiors of CuCrZr (HTB) either. The overall precipitate density was slightly lower as a result of the bonding thermal treatment, but in this case the precipitate size remained roughly the same (Table 3). The types of precipitates remained essentially unchanged between HTE and HTB specimens [6]. TEM of the HTC′ (E + bakeout) specimens revealed a slight decrease in the density of the precipitates and no other discernible changes were observed.

The precipitate reactions that occur in CuCrZr are not clearly understood, but it appears that at least two types of precipitates were formed during the prime aging treatment. Small G–P zones are present that exhibit a lobe–lobe appearance with a line of no contrast perpendicular to the operating $(200)_{Cu}$ reflection, an appearance known to occur for very small, coherent spherical particles [8]. The average size of these G–P zones, estimated by measuring the length of the line of no contrast (LONC), is 2.3 nm. The size distributions for the precipitates are given in Fig. 8. The diffraction patterns from the prime aged CuCrZr revealed no discrete diffraction spots from either the G–P zones or the fringed precipitates [6]. Streaking is observed around the {200} reflections in the ⟨220⟩ directions, a consequence of shear strains along the ⟨110⟩ directions in the copper lattice as proposed by Tang et al. [9].

There were other precipitates present in the microstructure that differed from the G–P zones in both size and appearance. These precipitates tended to exhibit Moiré fringes when imaged using a $g = [200]_{Cu}$ reflection. However, many precipitates were not clearly visible. These fringed precipitates are thought to be incoherent because of the lack of any strain fields around them. The fringed precipitates were oriented in three different directions, suggesting that they may be the same type of precipitate but with more than one orientation relationship or habit plane visible in the image. The size distribution of the fringed precipitates was not measured because of the uncertainty concerning the type and orientation, however, a qualitative estimate places the average size at 3–5 nm. The incoherent fringed precipitates may be Cr-rich precipitates, however, it is not clear whether they are a bcc or a metastable fcc as has been proposed in the literature [8–11]. The presence of the $CuZr_4$ phase was not observed. More detailed work is necessary to confirm the composition of the precipitates.

The fraction of precipitates exhibiting the G–P zone contrast and those with a fringed appearance is ~ 50% of each, and this ratio changes only a little with the heat treatment. All of the precipitates are thought to be spherical because tilting to different orientations did not reveal any edge-on platelets. Imaging the same area using first a $(200)_{Cu}$ and then a $(220)_{Cu}$ reflection showed that the G–P zones changed from the lobe–lobe appearance in the $(200)_{Cu}$ image to that of circular precipitates in the $(220)_{Cu}$ images.

3.1.3. CuAl25 (HTD only)

The annealing of CuAl25 (as-wrought) at 950°C for 30 min (corresponding to the joining thermal cycle) did not have any noticeable effect on dislocation or particle microstructures [6]. The oxide dispersion in the as-wrought CuAl-25 consisted of particles primarily of spherical or polygonal morphologies with an average size of ≃ 8 nm. The number of triangular particles was found to be very small in this particular heat of material (Fig. 7). Note also that the oxide particles shown in the figures vary in both size and number density, which is related to the inhomogeneity in the microstructure (see [12]). The particles have a cube-on-cube orientation relationship with the copper matrix, with an average density of 8.8×10^{22} particles/m^3.

3.2. Post-irradiation microstructure

The most pronounced effect of irradiation is observed in the solution annealed (i.e., HTA) specimens of both

CuCrZr and CuNiBe alloys. Prior to irradiation, no precipitates other than the large primary particles were visible in the solution annealed specimens. TEM investigations of the irradiated specimens, on the other hand, showed the presence of a dense population of small coherent precipitates in both alloys. All three alloys exhibited no evidence of void swelling. It should be noted here that the OFHC–copper irradiated under the same conditions as these alloys (i.e., at 250°C to 0.3 dpa) showed a swelling level of 0.13%) [13]. The microstructures for each of the alloys in the different heat treatments are described in the following sections.

3.2.1. CuNiBe

The post-irradiation specimens of the solution annealed CuNiBe (HTA) were found to contain a high density of small G–P zones not present in the unirradiated specimens (Fig. 8, Table 3). The precipitates are so small and densely populated that the overlapping strain fields from both the precipitates and the defect clusters made the characterization of their density and size distribution rather difficult. However, the precipitate density in the solution annealed and irradiated CuNiBe was estimated from the matrix dark field images and was found to be lower than that in the prime aged CuNiBe before irradiation (see Table 3). γ''-phase may be present, but the diffraction patterns do not reveal any discrete reflections. Given the size of the precipitates and the streaking in the diffraction patterns, it is thought that the visible precipitates are in fact G–P zones.

The size of the G–P zones in the irradiated solution annealed (HTA) specimens could not be determined with confidence. Attempts to image the G–P zones in precipitate dark field, i.e., using the streaks to image the precipitates, did not clearly distinguish the precipitates. The diffraction patterns showed the same ⟨001⟩ streaking [6], but in the solution annealed case the streaks were much fainter. The reason for this is not clear, though it may be related to a lower volume fraction of the precipitates. Although the matrix dark field imaging revealed a fraction of the precipitates, the overlapping strain contrast from the G–P zones and the defect clusters prevented an accurate measurement of the size of the G–P zones. Qualitatively, it appears that the G–P zones in the irradiated solution annealed (HTA) specimen are smaller than those observed in the unirradiated and irradiated HTE and HTB CuNiBe specimens. The characteristics of the defect clusters could not be determined either for the reasons just mentioned, however, they were visible among the G–P zones. TEM examination of the grain boundaries revealed precipitate denuded zones along the grain boundaries, as well as the presence of a low density of small precipitates directly on the boundaries (Fig. 8).

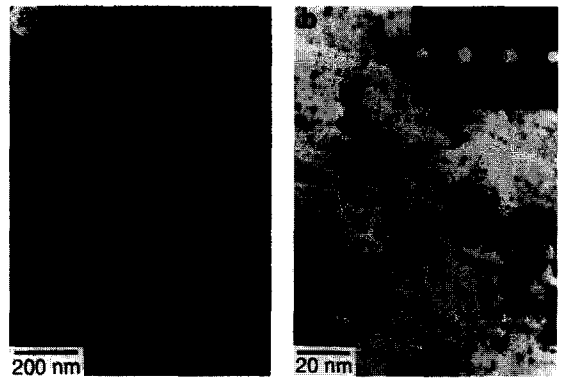

Fig. 8. Post-irradiation microstructure of the solution annealed CuNiBe (HTA) showing (a) the presence of denuded zones along a grain boundary and (b) much smaller, less distinct G–P zones in the grain interior. The diffraction pattern insert in (b) shows faint streaking, evidence of the low volume faction of the G–P zones.

Irradiation at 250°C produced less drastic changes in the CuNiBe specimens that were given the HTB and HTE heat treatments prior to irradiation. The denuded zones are still present after irradiation in both the HTB and the HTE specimens. However, the zone is not as clearly defined as it was in the unirradiated specimen (Fig. 9a) because of a more gradual gradient in the density of small precipitates in the denuded zone. This is in contrast to the denuded zones observed in the unirradiated specimens, which had a much more sharply defined transition. The formation of precipitates in the denuded zone after irradiation provides the evidence for the radiation-induced precipitation in the denuded zones, and presumably in the interiors of the grains. The grain boundary precipitates are still very much in evidence, as well as the large precipitates in the interior of the grains. The mean size of the G–P zones and that of the γ'' precipitates are quoted in Table 3. Note that the HTB specimens experienced the largest change in precipitate size with the density decreasing by a factor of 2. The size distributions of the HTB specimens (Fig. 2) show that the mean size has shifted after irradiation to a smaller

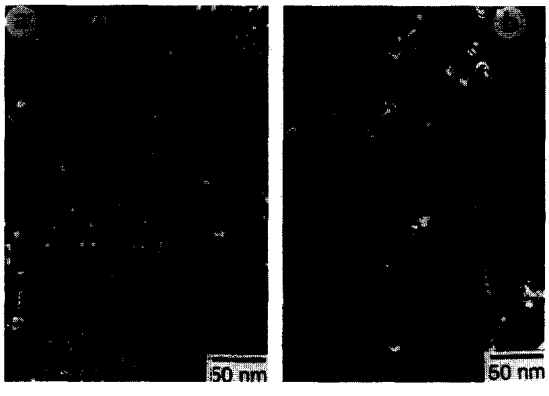

Fig. 7. Microstructure of the unirradiated CuAl-25 (HTD) showing oxide particles imaged using weak beam dark field on the $[200]_{Cu}$ reflection. Note the difference in particle size and density between (a) and (b).

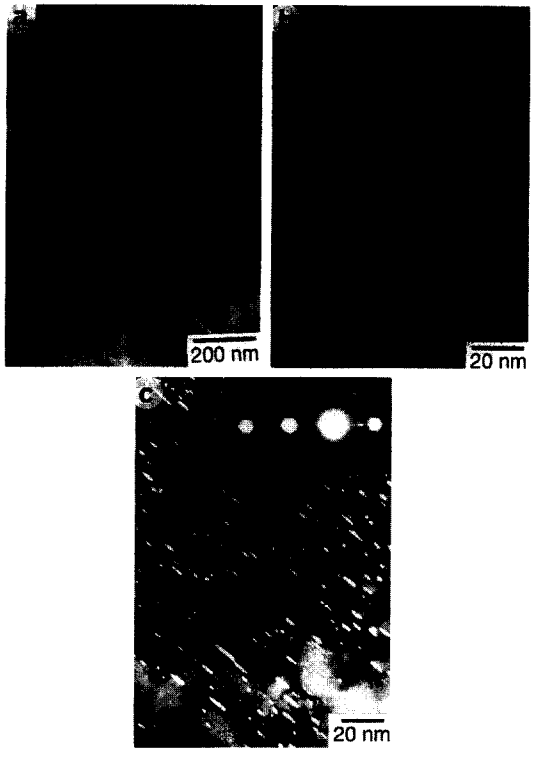

Fig. 9. Post-irradiation microstructure of the CuNiBe (HTB) specimens showing (a) denuded zones along a grain boundary demonstrating the presence of small precipitates formed during irradiation, (b) precipitates and defect clusters (e.g., SFTs) and (c) precipitates in the grain interior.

mean size (6.6 → 5.0 nm), however, the overall range of precipitate sizes still extends up to above 15 nm. In contrast to this, the precipitates in the HTE specimens remained roughly the same in size, but here again the density decreased significantly. The shift in mean size in the HTB specimens brings the precipitate size down to those measured for the HTE specimens, suggesting that radiation-induced dissolution and re-precipitation of the precipitates is producing a similar microstructure in both heat treated conditions, independent of the initial starting state.

The defect clusters could not be easily distinguished in the irradiated HTE specimens because of the high density of G–P zones, although they were seen in some areas of the HTB specimens, e.g., Fig. 9b. Though it is clear that the defect clusters are present in these specimens, the actual size and number density could not be determined to see if there is any influence of alloying elements on the defect cluster characteristics. An example of the precipitate microstructure in the irradiated CuNiBe with the HTB heat treatment is shown in Fig. 9c.

3.2.2. CuCrZr

While the CuNiBe has shown itself to be sensitive to irradiation from a microstructural standpoint, the CuCrZr

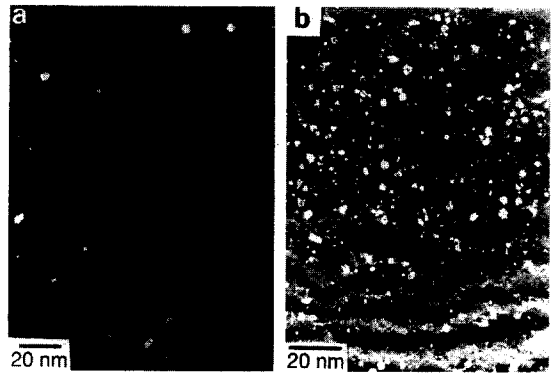

Fig. 10. Post-irradiation microstructure of the CuCrZr (HTE) specimens, revealing (a) the mixture of incoherent fringed particles and (b) small white dots, and SFTs.

tends not to be as susceptible. The data given in Table 3 show that irradiation of CuCrZr has a minimal effect when compared to the changes in CuNiBe. The precipitate density data in both the unirradiated and the irradiated specimens include all types of precipitates. In the irradiated specimens of all three heat treatment conditions (HTA, HTB, and HTE), a large fraction of the precipitates were visible only as small white dots (1–4 nm) in the weak beam dark field images [6]. This was more common in the case of the solution annealed CuCrZr, where the microstructural features did not correspond to either the fringed particles or the G–P zone type of precipitates. Though it is possible that a portion of these might be defect clusters, it is known from examinations of other copper specimens that most of the visible defect clusters in thin sections of the foil (< 40 nm thickness) are SFTs, which have a characteristic triangular appearance when imaged using $g = [200]_{Cu}$ [13]. Therefore, the small white

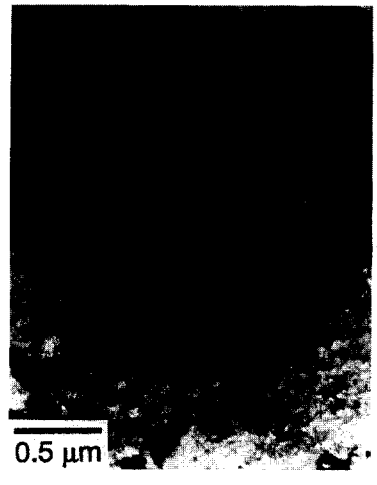

Fig. 11. Post-irradiation microstructure of the CuCrZr (HTB) specimens showing dislocation loop microstructure.

dots are thought to be very small precipitates, possibly G–P zones of a different type than normally seen in these alloy.

The sizes given for the precipitates (Table 3) in the irradiated HTB and HTE CuCrZr specimens cannot be directly compared to their unirradiated counterparts. In the unirradiated specimens a mixture of incoherent fringed particles and G–P zones was described previously, with the size distributions measured for the G–P zones only (lobe–lobe type). A qualitative estimate of the size was made from the micrographs, however, and placed the size range of the fringed precipitates at 3–5 nm. In the irradiated specimens the G–P zones are completely absent, and are replaced by a mixture of incoherent fringed particles (mean sizes listed in Table 3) and the smaller precipitates not yet identified (Fig. 10). The fringed precipitates are more numerous and more clearly defined than that in the unirradiated specimens. The size distributions given in Fig. 8 for the irradiated specimens are for the incoherent fringed particles, and yield an average size of 4–5 nm depending on the heat treatment, which matches the qualitative estimate obtained from the unirradiated specimens. The uncertainty regarding the orientation relationship and habit planes holds true in the irradiated specimens also, so the number density should be viewed with caution since all of the precipitates may not be visible at this orientation.

In summary, irradiation of CuCrZr in the solution annealed (HTA) state resulted in the formation of a high density of small precipitates, possibly G–P zones of a different type, possessing a different appearance than typically observed in the unirradiated and irradiated HTB and HTE specimens. After irradiation the precipitates in these latter specimens changed from a mixture of G–P zones and fringed particles to a mixture of fringed particles and the small unidentified precipitates observed in the irradiated solution annealed specimen. Denuded zones were not observed in the irradiated CuCrZr alloys, nor were there any evidence of significant precipitation at the grain boundaries.

Fig. 12. Microstructure of the irradiated CuAl-25 (HTD), showing defect clusters (e.g., SFTs).

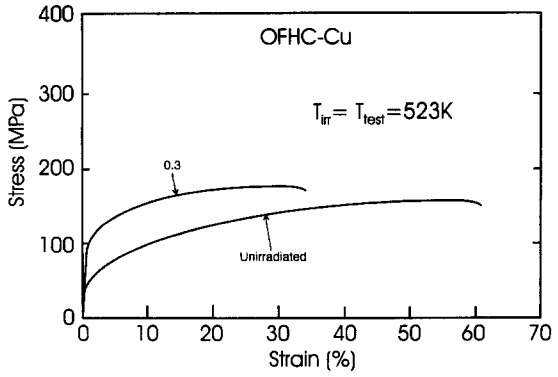

Fig. 13. Tensile curves for OFHC copper before and after irradiation at 250°C, demonstrating the large increase in strength and decrease in ductility.

One microstructural feature that bears mentioning is the formation of a network of dislocation loops in the irradiated CuCrZr (Fig. 11). In comparison, no such loop formation was observed in pure copper irradiated at 250°C to $\simeq$ 0.3 dpa, nor in the CuNiBe and CuAl-25 alloys. It is interesting to note in this context that the formation of dislocation loops has been also observed in binary alloys such as Cu–5% Mn and Cu–5% Ni irradiated with 750 MeV protons at 160°C and 90°C, respectively, to dose levels of 1.6 and 0.7 dpa [14]. No loops were observed in pure copper irradiated with 750 MeV protons to a dose level of 0.7 dpa at 90°C. In the case of the CuNiBe, the G–P zones dominate the microstructure to the point that it is impossible to characterize any microstructural features other than G–P zones and large SFTs. Therefore, it may be possible that dislocations loops have formed, but simply are not visible.

3.2.3. CuAl-25 (HTD only)

As shown in Fig. 12, no visible change occurred in the oxide dispersion, the dislocation structure or the grain structure. The density of the particles is significantly lower than that measured for the unirradiated specimens (Table 3). However, previous studies by Singh and co-workers [12] showed that the GlidCop class of alloys possessed a heterogeneous distribution of oxide particles when examined at the scale of the grain structure. Depending on the location chosen, the oxide particle density was found to vary by as much as a factor of 10 or more (10^{22}–10^{23} particles/m^3). Therefore, the lower particle density measured for the irradiated specimens may be a result of the heterogeneity in the oxide dispersion, and not a consequence of the irradiation.

Table 4
Results of electrical resistivity measurements at room temperature for un-irradiated and irradiated copper alloys after different heat treatments (pre-irradiation). Irradiation was performed at 250°C. The relative resistivity is the resistivity normalized to the resistivity value measured for annealed OFHC–copper

Materials	Heat treatment	Irradiation dose (dpa)	Relative resistivity [b] (RR)	Relative conductivity (%)
OFHC–Cu	550°C/2 h	0	1.000	100
CuCrZr	A	0	2.09–2.16	46–48
CuCrZr	E	0	1.63–1.90	53–61
CuCrZr	B	0	1.40–1.73	58–71
CuCrZr	C	0	1.24–1.77	79–81
CuCrZr	C′	0	1.37–1.57	64–73
CuNiBe	A	0	2.96–3.23	31–34
CuNiBe	E	0	2.02–2.35	43–50
CuNiBe	B	0	2.01–2.38	42–50
CuNiBe	C	0	1.83–2.04	49–55
CuNiBe	C′	0	1.91–2.15	47–52
CuNiBe	CA [a]	0	1.55	65
CuNiBe	CK [a]	0	1.46	68
CuAl-25	D	0	1.13	88
CuAl-25	D′	0	1.15	87
CuCrZr	A	0.3	–	–
CuCrZr	E	0.3	1.52	66
CuCrZr	B	0.3	1.48	68
CuNiBe	A	0.3	3.22	31
CuNiBe	E	0.3	2.33	43
CuNiBe	B	0.3	2.22	45
CuNiBe	CA	0.3	1.87	53

[a] Specimens from Oak Ridge National Laboratory, material originally from Brush Wellman, Cleveland, OH; heat number 33667.
[b] A range of values show the measured variation in resistivities between different batches of samples with the same nominal heat treatment.

Defect clusters, predominantly SFTs were found in a random distribution throughout the grains. The images of the SFTs are square, and not triangular as would occur if they were imaged near an ⟨011⟩ zone axis on a $g = [200]$ condition. Their density in the DS copper is roughly 2.5 times lower than that measured for the CuCrZr, but whether this is due to the moderately heavy dislocation structure or to the presence of the oxide particles remains unknown.

3.3. Pre- and post-irradiation electrical resistivity

For comparison, resistivity measurements were carried out on unirradiated specimens with nominally the same heat treatments but carried out in different batches. The relative resistivity (RR) values for the various alloys quoted in Table 4 are the average values of six measurements made on each specimen. These measurements showed small variations in resistivity as shown in Table 4. The results on the unirradiated CuNiBe show that the HTB and HTE treatments cause a decrease in the resistivity as expected (see Table 4). Note, however, that the resistivity of the Tréfimétaux CuNiBe is much higher than that of two heats of Hycon 3HP® CuNiBe supplied by Brush Wellman (USA), another producer of CuNiBe alloys. The compositions and processing of the Brush Wellman heats have been optimized to yield a lower electrical resistivity while maintaining a reasonably high level of strength, though not as high as that of the Tréfimétaux CuNiBe. The relatively high resistivity of the Tréfimétaux CuNiBe suggests that a fraction of the beryllium and/or nickel (or other impurities) may still be in solid solution, and that the composition and thermal processing have yet to be optimized. In addition, note that the bakeout treatment had relatively little effect on the resistivity of the Tréfimétaux CuNiBe, indicative of the relative stability of the microstructure even when annealed at 350°C for 100 h.

Table 5
Tensile results for OFHC–copper in the unirradiated and irradiated (at 250°C to 0.3 dpa) conditions

Material	Heat treatment	Dose (dpa)	$\sigma_{0.05}$ (MPa)	$\sigma_{0.2}$ (MPa)	σ_{max} (MPa)	ε_u^p (%)	ε_{total} (%)
OFHC	550°C/2 h	0	34	38	162	54.5	60.5
OFHC	550°C/2 h	0.3	90	100	174	32.0	34.0

Table 6
Tensile results for unirradiated copper alloys with the pre-irradiation heat treatments described in Table 2. Tests were conducted at 250°C

Material	Heat treatment	$\sigma_{0.05}$ (MPa)	$\sigma_{0.2}$ (MPa)	σ_{max} (MPa)	ε_u^p (%)	ε_{total} (%)
CuCrZr	A	52	56	177	33.0	36.0
CuCrZr	B	94	100	219	27.3	31.3
CuCrZr	C	171	181	274	17.2	20.4
CuCrZr	C′	208	218	308	15.9	20.3
CuCrZr	E	135	140	261	22.6	25.5
CuNiBe	A	173	178	325	47.5	54.0
CuNiBe	B	455	480	665	24.6	30.5
CuNiBe	C	540	580	750	20.5	27.0
CuNiBe	C′	565	600	780	13.7	17.5
CuNiBe	E	505	558	734	13.8	16.8
CuAl-25 [a]	D	306	315	326	1.5	18.5
CuAl-25 [a]	D′	270	280	294	2.2	15.5
CuNiBe (Hycon) [b]	Similar to HTE	640	690	730	3.0	5.3

[a] Round tensile geometry only.
[b] Longitudinal direction, heat number 33667.

Comparing the electrical resistivity of the Tréfimétaux CuNiBe (HTC) with that of the particle density quoted in Table 3, the decrease in the particle density did not lead to any substantial decrease in electrical resistivity. In fact, the difference in precipitate density between the HTE and HTB specimens is barely reflected in the electrical resistivity.

The irradiation of these alloys had little effect on the electrical resistivity. However, given that the precipitate density and size experienced considerable change after irradiation, it is likely that the ballistic dissolution and re-precipitation still leave solute elements in solid solution.

The CuCrZr specimens exhibited a lower resistivity than the CuNiBe alloys in each of the 5 heat treatments. In contrast to the CuNiBe, the bakeout treatment given to the CuCrZr HTB specimen (HTC) clearly lowered the resistivity. Unlike the CuNiBe, irradiation improved the electrical resistivity of the CuCrZr alloy, but even this improvement still left the resistivity significantly higher than that of the CuAl-25 alloy. The improvement in resistivity of the CuCrZr after irradiation suggests that irradiation led to coarsening and possibly additional precipitation that drove the remaining solute elements out of solution, which agrees qualitatively with the TEM results. The results bear out the superior electrical resistivity of the CuAl-25 under these irradiation conditions. Transmutation effects are assumed to be minor for this low dose.

3.4. Mechanical properties

The mechanical properties of the three alloys show that irradiation can have a strong influence on the strength and ductility, with the CuNiBe showing the strongest susceptibility to irradiation effects. The results for the individual alloys are summarized in the following sections, and the tensile data for the pure copper and copper alloys are listed in Tables 5–7.

Table 7
Tensile results for copper alloys irradiated at 250°C to 0.3 dpa with the pre-irradiation heat treatments described in Table 2. Tests were conducted at 250°C

Material	Heat treatment	$\sigma_{0.05}$ (MPa)	$\sigma_{0.2}$ (MPa)	σ_{max} (MPa)	ε_u^p (%)	ε_{total} (%)
CuCrZr	A	195	205	205	0.4	2.5
CuCrZr	B	215	224	223	4.0	5.0
CuCrZr	E	230	235	254	4.2	7.0
CuNiBe	A	590	655	670	0.6	1.9
CuNiBe	B	565	630	685	0.7	1.8
CuNiBe	E	625	690	705	0.3	1.5
CuAl-25 [a]	D	280	303	328	1.8	15.3
CuAl-25 [a]	D′	285	308	320	1.6	13.8
CuNiBe (Hycon) [b]	Similar to HTE	530	620	655	1.0	3.1

[a] Round specimen geometry only.
[b] Longitudinal direction, heat number 33667.

3.4.1. Pure copper

For comparison with the properties of the unirradiated and irradiated alloys, representative tensile curves demonstrating the tensile behavior at 250°C for OFHC–copper are shown in Fig. 13, and the tensile data are quoted in Table 5. At 250°C, the increase in yield strength is approximately a factor of three at the dose of 0.3 dpa, whereas the ultimate strength is relatively unchanged. Along with the increase in yield strength, there is a decrease in work hardening as well as in uniform and total elongation.

3.4.2. CuNiBe

The tensile results for the unirradiated CuNiBe specimens are provided in Fig. 14 and Table 6, and show that the heat treatment (HTC′) yields the highest strength. The solution annealed material possesses a higher yield strength compared to the annealed pure copper (Fig. 13), presumably due to the effect of solid solution strengthening. The HTB specimens exhibit a lower overall strength and higher ductility than the HTE specimens, which is not surprising since the heat treatment B produces a coarser microstructure than the heat treatment E. It is significant to note that the grain boundary denudation prevalent in the HTB specimens did not have any deleterious effect on the mechanical properties, particularly the ductility.

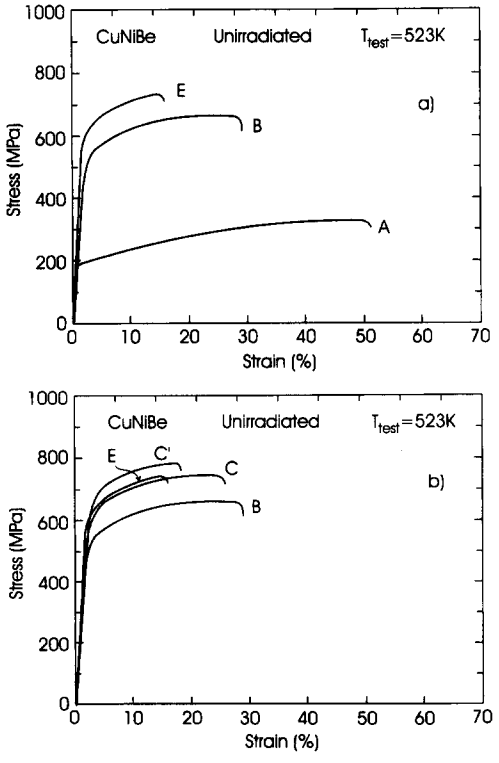

Fig. 14. Tensile curves showing the influence of the different heat treatments on the deformation behavior of the CuNiBe alloy. The curves in (b) illustrate the effect of the bakeout treatment (HTC).

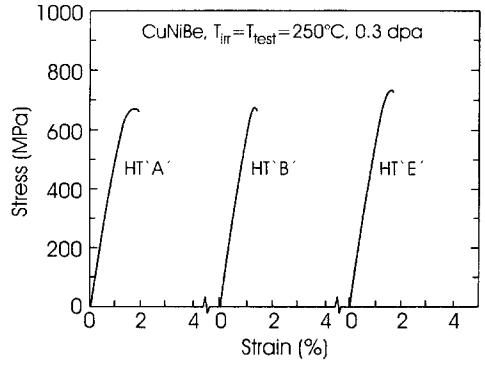

Fig. 15. Tensile curves for the irradiated CuNiBe showing the severe loss of ductility after irradiation, regardless of the pre-irradiation heat treatments. Note that the post-irradiation strength of the solution annealed CuNiBe (HTA) is similar to that of the irradiated CuNiBe with the HTE and HTB heat treatments.

The bakeout simulation (HTC) actually increases the strength somewhat. The exact cause for this is uncertain at this time, because compared to the HTB specimens, there was little change in the microstructure to account for the increase in strength. It may be that the bakeout treatment, essentially a low temperature aging treatment, produces a finer dispersion of precipitates that cannot be seen in the microstructural analysis. The effect of the bakeout simula-

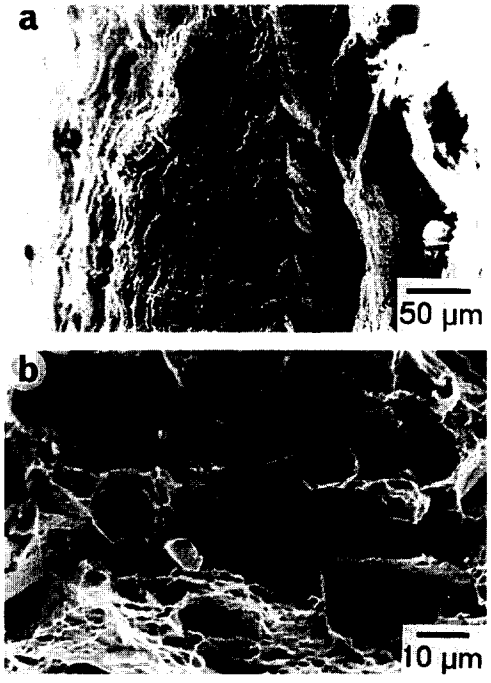

Fig. 16. Fracture surfaces of the solution annealed CuNiBe (HTA) in (a) the unirradiated condition and (b) after irradiation. Note the intergranular cleavage at the grain boundary facets of the fracture surface in the irradiated specimen.

tion on specimens initially given the heat treatment E is just the opposite, that is, the strength actually decreases somewhat. These results agree qualitatively with the microstructural results which show that the microstructure coarsens during the bakeout treatment.

Irradiation of these alloys reveals that the Tréfimétaux CuNiBe suffers a severe loss of ductility after irradiation (Fig. 15, Table 7). The solution annealed specimens exhibit a large increase in strength (178 vs. 655 MPa), but this is also accompanied by a large loss of ductility compared to the unirradiated state. The strength of the solution annealed specimens after irradiation is comparable to the specimens given the HTB and HTE treatments, indicative of the strong effect of irradiation-induced precipitation in these alloys. The differences in strength between the HTB and HTE are no longer as apparent despite the differences in precipitate density. Part of this may be masked by the poor ductility ($\leq 1\%$ ε_u^p for all three heat treatments) which prevents the alloy from exhibiting any work hardening. The fracture surfaces of these alloys, as shown in Fig. 16, reveal that the failure mode has changed from a completely ductile mode in the unirradiated state to a mixture of ductile intergranular and intergranular cleavage, suggesting that the grain boundaries have been weakened during irradiation.

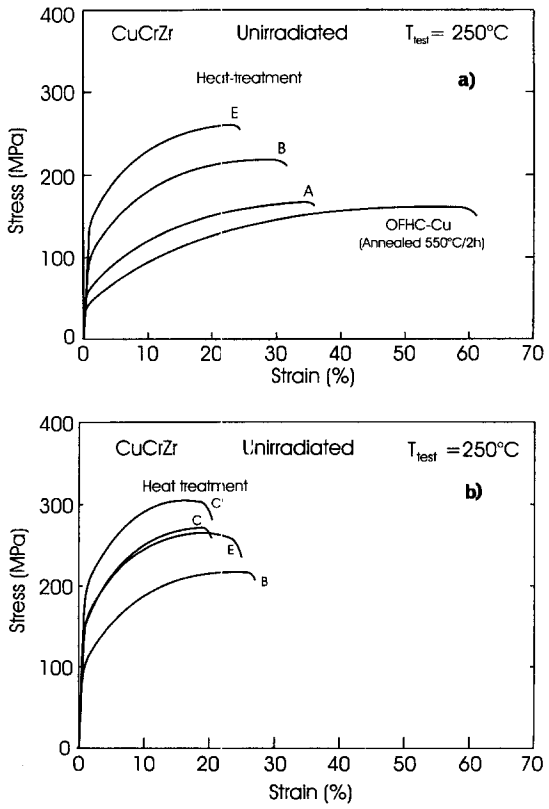

Fig. 17. Tensile curves showing the influence of different heat treatments on the deformation behaviour of CuCrZr and how they compare to annealed pure copper. The curves in (b) illustrate the effect of the bakeout treatment.

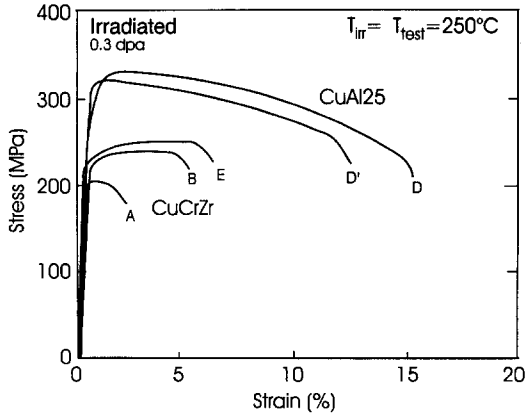

Fig. 18. Comparison of the tensile behavior of CuCrZr to that of CuAl-25 after irradiation at 250°C to 0.3 dpa. Note that the CuCrZr still retains a measurable ability to work harden, whereas the CuAl-25 shows a very limited amount of work hardening.

For comparison, specimens of a commercial CuNiBe (Hycon 3HP®) manufactured by Brush Wellman (USA) were also irradiated at 250°C to a dose level of 0.3 dpa and subsequently tested at 250°C (see Table 7 for tensile results). The material was in a fully hardened tempered condition (referred to as the HT temper in the United States), but the exact conditions are held proprietary by Brush Wellman. However, the HT temper normally involves solution annealing, cold working, and then aging for several hours. The pre-irradiation microstructure of the Hycon 3HP® CuNiBe is significantly coarser than that observed in the Tréfimétaux CuNiBe with the heat treatment HTE. The difference is probably due to the different aging treatments. It is not surprising therefore, that the CuNiBe (Hycon) exhibits somewhat lower yield strength and higher ductility than those measured in the Tréfimétaux CuNiBe (HTE) (see Ref. [15] for a detailed comparison). The results on CuNiBe (Hycon) reported in Table 7 are similar to those reported by Zinkle and Eatherly [16]. It should be emphasized here that it is not known how the Hycon 3HP® alloy would respond to the bonding thermal cycle (HTB), subsequent irradiation and post-irradiation mechanical testing.

3.4.3. CuCrZr

The tensile curves shown in Fig. 17 and the data listed in Table 6 for CuCrZr illustrate the differences that arise due to the 5 different heat treatments. The solution annealed CuCrZr does not exhibit the same degree of solution hardening as the solution annealed CuNiBe. In fact, its yield strength is very close to that annealed OFHC–copper, but with noticeably less ductility. The aging temperature and time used in the HTE and HTB heat treatments produces an underaged microstructure in CuCrZr. The lack

of cold work prior to aging also leads to less precipitation, further lowering the strength. Note that cold working prior to aging in the case of the CuNiBe alloy is not required to achieve high strength. All three heat treatments result in a material that possesses a high degree of work hardening, which the CuNiBe exhibits to a lesser extent, and is almost non-existent for CuAl-25 at 250°C.

CuCrZr responds differently to the bakeout treatments than the CuNiBe. In both cases the bakeout treatment (or extra aging) resulted in a significant increase in strength over the original starting state, and with little change in ductility. This would indicate that the heat treatment E is not sufficient to obtain maximum precipitation hardening. This may be related to the lack of cold work prior to aging, and the slower diffusion of the Cr in copper.

The irradiated CuCrZr results are shown in Fig. 18 and listed in Table 7. Clearly the irradiation of the solution annealed specimens has produced the same effect as in the CuNiBe, that is, radiation-induced precipitation that effectively doubles the strength. Irradiation of the other two heat treatments results in a large increase in yield strength, but little change in the ultimate strength. However, unlike the CuNiBe, this alloy still possesses a moderate amount of ductility in the HTB and HTE conditions, and retains some ability to work harden. The solution annealed condition has the lowest uniform elongation of the three irradiated conditions, and very little work hardening ability. The fracture surfaces for the CuCrZr show that before and after irradiation it still has a ductile failure mode, exhibiting a 'knife edge' fracture surface due to the large reduction in area.

3.4.4. CuAl-25

The effect of annealing at 950°C for 30 min. (HTD) on the flow stress of CuAl-25 is found to be very small (Table 6). It should be pointed out that unlike CuCrZr and CuNiBe alloys, the CuAl-25 does not seem to work-harden during tensile deformation at 250°C (Fig. 18). Tensile curves comparing the unirradiated and irradiated CuAl-25 are shown in Fig. 19, and again show that little change occurs after irradiation. As in the unirradiated specimens, irradiated CuAl-25 exhibits little ability to work harden, which raises questions about its fracture toughness and resistance to crack growth. The apparent lack of any effect of the annealing and irradiation is reflected in the microstructural response, which also showed no discernible difference. The fracture surfaces yield little information outside of the failure mode being ductile in nature, primarily because the grain size is too small to allow one to distinguish transgranular or intergranular failure.

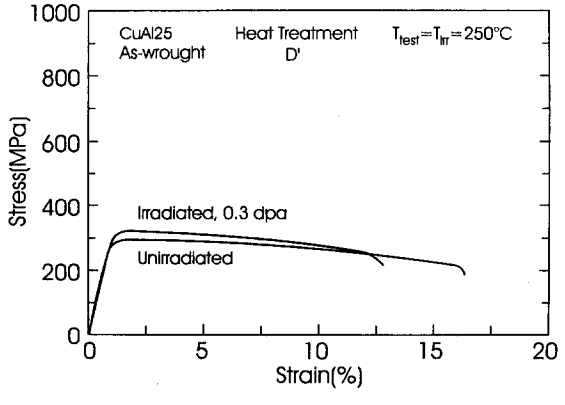

Fig. 19. Tensile behavior of CuAl-25 demonstrating that the irradiation at 250°C does not seem to cause any hardening.

4. Summary

Of all the alloys, CuAl-25 proves to be the most stable in terms of the microstructure, mechanical properties and electrical resistivity. The bonding thermal treatment should have little effect on the properties or microstructure of the DS copper alloys. Although irradiation may lead to minor changes in the oxide dispersion, mostly by altering the particle morphology, in general the dislocation structure, oxide dispersion, and grain structure are not significantly influenced by neutron irradiation at the low dose of 0.3 dpa. The apparent lack of work hardening ability, which is also absent in CuNiBe (but for different reasons), is a matter of concern.

The CuCrZr appears to be less susceptible to neutron irradiation effects at 250°C than CuNiBe, and still retains some ability to work harden after irradiation. The various heat treatments given to the CuNiBe have little effect on the response of the alloy to irradiation. The CuCrZr, regardless of the initial heat treatment, exhibits a general increase in strength after irradiation, but with sufficient ductility to warrant further consideration for its use at 250°C. Similar results have been reported earlier by Fenici et al. [17] for a commercial CuCrZr alloy (Elbrodur) irradiated with fission neutrons at 255°C to a dose level of 10 dpa. The obvious disadvantage with the CuNiBe alloys lies in the lack of ductility after irradiation and testing at 250°C. This is in contrast to the mechanical properties that were measured after irradiation at 47°C [12], where the CuNiBe still possessed measurable uniform elongation and the highest strength of the three candidate alloys. The irradiation-induced loss of ductility associated with all three heat treatments raises serious concerns about the fracture toughness of this material.

The poor behavior of the CuNiBe after irradiation may be due to segregation at the grain boundaries, although there is not enough evidence to confirm this. Irrespective of the initial state, the fracture surfaces revealed that failure occurred near or at the grain boundaries, and not within the bulk of the grains. This weakening of the grain boundary regions in a manner that allows all of the defor-

mation to occur at the boundaries, and not in the interior of the grains, may be related to segregation of Be or Ni (or perhaps impurity elements) to the grain boundaries during irradiation. It may also be that the presence of precipitates and irradiation-induced damage make the grain interiors significantly stronger than the grain boundaries and the precipitate denuded zone along the boundaries. This difference may allow the initiation and localization of the plastic flow in the grain boundary region, leading to separation of the grains without any significant amount of plastic deformation within the grain interiors.

Regardless of the precipitate size and density, the post-irradiation strengths of the HTA, HTB, and HTE CuNiBe were very similar. This suggests that dissolution and re-precipitation of the small G–P zones and γ'' precipitates may be occurring to produce a precipitate microstructure that eventually will be very similar for all three alloys. The average size of the precipitates in both HTB and HTE specimens appears to be changing during irradiation to a size common to both heat treatments, effectively eliminating any differences due to the initial starting state. The lack of any significant change in the electrical resistivity of the HTB and HTE specimens after irradiation may be the result of the dissolution and re-precipitation, which leaves a certain level of Be and Ni in solution.

The CuCrZr exhibited a similar behavior in that the HTB and HTE specimens possess approximately the same strength after irradiation, indicating again that radiation-induced precipitation is playing a role in determining the response to irradiation. In both alloy systems (CuCrZr and CuNiBe) it is clear that the role of the initial starting state has little effect on the final mechanical properties, even at a low dose of 0.3 dpa. The increase in yield strength observed for the HTB and HTE specimens of CuCrZr, along with the increase in conductivity, would indicate that irradiation resulted in further precipitation and coarsening that removes excess Cr and Zr from solution. Because of the different diffusion kinetics and the limited solubility of Cr in copper, the CuCrZr alloys respond differently to irradiation than the CuNiBe. Another example of this difference is the formation of a high density of large dislocation loops (> 10 nm) that normally do not occur in pure copper. In this alloy the Cr and/or Zr are clearly acting to influence the formation of dislocation loops. This has not been observed in the CuNiBe because the high precipitate density.

5. Conclusions

On the basis of the changes measured in the microstructure, mechanical properties, and electrical resistivity, the following conclusions can be drawn.

- The DS copper alloy CuAl-25 exhibits the greatest resistance to radiation-induced changes in microstructure and mechanical properties at 250°C.
- The different heat treatments given to the CuNiBe and CuCrZr made little difference in the mechanical properties after irradiation at 250°C to 0.3 dpa.
- Irradiation of solution annealed CuNiBe and CuCrZr leads to radiation-induced precipitation which increases the strength levels near to that of the HTB and HTE specimens.
- The two precipitation strengthened alloys (i.e., CuNiBe and CuCrZr) are susceptible to changes in the microstructure that can affect their mechanical properties.
- Radiation-induced dissolution and re-precipitation change the precipitate characteristics in both CuNiBe and CuCrZr alloys. In addition, the radiation-induced precipitate dissolution may be responsible for promoting segregation of alloying elements in the CuNiBe, particularly at grain boundaries.
- CuCrZr appears to offer advantages over the CuNiBe because there remains a reasonable level of ductility and work hardening even after irradiation.
- The severe loss of ductility in the CuNiBe alloy due to neutron irradiation, regardless of the initial starting state, poses a serious concern for this alloy, particularly since the actual mechanism responsible for the poor behavior remains unclear.
- The strong sensitivity of the microstructure and mechanical properties of CuNiBe alloys to irradiation with fission neutrons may present serious problems regarding their application in an intense flux of 14 MeV neutrons. The situation is made worse since the actual mechanism(s) responsible for the observed decrease in ductility in the post-irradiation CuNiBe alloys has not been firmly identified.

Acknowledgements

The present work was partly funded by the European Fusion Technology Programme. The authors wish to thank B.F. Olsen, N.J. Pederson and J.L. Lindbo. D.J.E. would like to thank Risø National Laboratory for the support and assistance during his visit. His work was also partly supported by the US Department of Energy under contract DE-AC06-76RLO 1830 with the Battelle Memorial Institute at the Pacific Northwest National Laboratory. The authors would like to thank Dr S.J. Zinkle for supplying tensile specimens of CuNiBe (Hycon) (heat No. 33667).

References

[1] ITER Joint Central Team, J. Nucl. Mater. 212–215 (1994) 3.
[2] J.W. Davies, D.E. Driemeyer, J.R. Haines, R.T. McGrath, J. Nucl. Mater. 212–215 (1994) 1353.
[3] S.J. Zinkle, A. Horsewell, B.N. Singh, W.F. Sommer, J. Nucl. Mater. 195 (1992) 11.
[4] D.J. Edwards, F.A. Garner, J.W. Newkirk, A. Nadkarni, J. Nucl. Mater. 212–215 (1994) 1313.

[5] S.J. Zinkle, E.V. Nesterova, V.R. Barabash, V.V. Rybin, A.V. Naberenkov, J. Nucl. Mater. 208 (1994) 119.
[6] B.N. Singh, D.J. Edwards, M. Eldrup, P. Toft, Risø-R-937 (EN), Jan. 1997.
[7] A. Guha, 'High conductivity copper and aluminum alloys', in: Conference Proceedings, eds. E. Ling and P.W. Taubenblat (The Metallurgical Society of AIME, Los Angeles, CA, 1984).
[8] M.F. Ashby, L.M. Brown, Philos. Mag. 8 (1963) 1083.
[9] N.Y. Tang, D.M.R. Taplin, G.L. Dunlop, Mater. Sci. Tech. 1 (1985) 270.
[10] Z. Rdzawski, J. Strobrawa, Scr. Metall. 20 (1986) 341.
[11] R.W. Knights, P. Wilkes, Metall. Trans. 4 (1973) 2389.
[12] B.N. Singh, D.J. Edwards, A. Horsewell, P. Toft, J. Nucl. Mater. 238 (1996) 244.
[13] B.N. Singh, A. Horsewell, P. Toft, D.J. Edwards, J. Nucl. Mater. 224 (1995) 131.
[14] S.J. Zinkle, A. Horsewell, B.N. Singh, W.F. Sommer, J. Nucl. Mater. 212–215 (1994) 132.
[15] B.N. Singh, D.J. Edwards, M. Eldrup, P. Toft, in preparation.
[16] S.J. Zinkle, W.S. Eatherly, Fusion Materials Semiannual Progress Report, DOE/ER-0313/20, 1996, p. 207.
[17] P. Fenici, D.J. Boerman, G.P. Tartaglia, J.D. Elen, J. Nucl. Mater. 212–215 (1994) 399.